Article

Machine Learning-Aided High-Throughput First-Principles Calculations to Predict the Formation Energy of μ Phase

Yue Su, Jiong Wang,* and You Zou

Read Online

ACCESS | Metrics & More | Article Recommendations

ABSTRACT: The μ phase is a type of hard and brittle constituent that exists in high-temperature alloys. The formation energy is a crucial thermochemical datum, and the accurate calculation of the formation energy of the μ phase contributes to the material design of high-temperature alloys. Traditional first-principles calculations demand significant computational time and resources. In this study, an innovative machine learning (ML)-based approach to accurately predict the formation energy of the μ phase is proposed. This approach involves the utilization of six algorithms and two model evaluation methods to construct the ML models. Leveraging a comprehensive data set containing 1036 binary configurations of the μ phase, the model trained using a 10-fold cross-validation technique, and the multilayer perceptron (MLP) algorithm achieves a mean absolute error (MAE) of 23.906 meV/atom. To validate

its generalization performance, the trained model is further validated on 900 ternary configurations, resulting in an MAE of 32.754 meV/atom. Compared with solely using traditional first-principles calculations, our approach significantly reduces the computational time by at least 52%. Moreover, the ML model exhibits exceptional accuracy in predicting the lattice parameters of the μ phase. The MAE values for the a and c parameters are 0.024 and 0.214 Å, respectively, corresponding to low error rates of only 0.479 and 0.578%. Additionally, the ML model was utilized to accurately predict the formation energy of all of the possible ternary configurations. To enhance accessibility to the formation energy data of the μ phase, a user-friendly graphical user interface (GUI) was developed, ensuring convenient usability for researchers and practitioners.
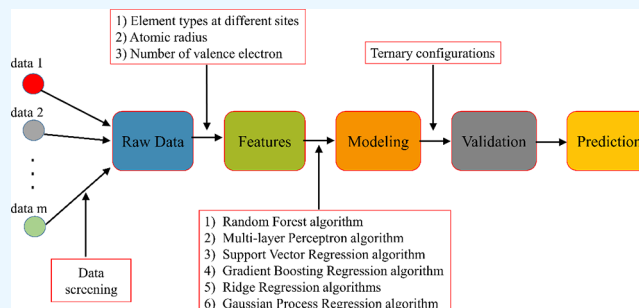
1. INTRODUCTION

High-temperature alloys are a class of materials that maintain high strength and heat resistance in high-temperature environments.[1−3] They are commonly used in the manufacturing of critical components in aerospace engines and gas turbines, such as turbine blades, turbine discs, and combustion chamber assemblies.[4] To enhance the performance of these alloys, the addition of refractory elements is a common practice. Common refractory elements include W, Mo, Nb, and Ta, which raise the alloy's melting point and thermal stability, thereby increasing its life span under high-temperature conditions.[5−9] However, the incorporation of these alloying elements can lead to the formation of detrimental topologically close-packed (TCP) phases during solidification, such as μ, σ, and Laves phases.[10,11] Of particular concern is the presence of the μ phase, a nonstoichiometric intermetallic compound commonly observed in Ni-based, Co-based, and Fe-based high-temperature alloys.[12,13] The formation of the μ phase can render the alloy brittle, reducing its plasticity and toughness. This can result in crack initiation and fracture under conditions of high stress and elevated temperature.[14,15] Precise control of the presence of the μ phase is necessary during the design and manufacturing of

high-temperature alloys to mitigate its adverse effects and achieve optimized material performance.

CALPHAD (calculation of phase diagram) simulation is widely recognized as one of the most effective tools in material design, as it enables quantitative predictions of phase equilibria in multicomponent alloys.[16,17] The existence of the μ phase in numerous alloy systems presents challenges for the experimental determination of phase boundaries. To employ the CALPHAD method for μ phase design, accurate thermochemical descriptions, including formation energy, are indispensable.[18−20]

First-principles calculations based on density functional theory (DFT) are commonly used for calculating the formation energy of the μ phase.[21,22] The μ phase is a hexagonal structure with 39 atoms occupying five inequivalent sites, namely 3a, 6c$_1$,

$6c_2$, $6c_3$, and 18h.[23−25] Composite energy formalism (CEF)[26] is typically employed in thermodynamic models to handle multicomponent and nonstoichiometric phases.[19] Nevertheless, calculating the formation energy of the μ phase is challenging due to the vast number of possible configurations. For example, two different elements can produce $2^5 = 32$ distinct configurations, three different elements can yield $3^5 = 243$ configurations, and four different elements can generate $4^5 = 1024$ configurations. The number of configurations rapidly increases with an increase in the number of elemental species. Therefore, relying solely on first-principles calculations for calculating the formation energy of the μ phase is impractical, as it would consume significant computational resources and time. Currently, a viable method involves combining machine learning (ML) with high-throughput first-principles calculations to address this issue.

Machine learning, a branch of artificial intelligence, has extensive applications in various fields. Unlike traditional computational science, ML aims to establish models based on analyzed data to automatically solve problems in unknown data sets.[27−30] In other words, machines can learn from past data and scenarios, improve algorithms, and make decisions when they encounter different or even unknown situations. Open-source ML packages such as scikit-learn, Keras, and PyTorch enable complete coding with just a few lines of Python. With the release of these software packages, ML has become more user-friendly. In this study, the formation energies of 1036 binary configurations and 900 ternary configurations were computed using first-principles calculations. The formation energy of binary configurations was used to construct the ML model, which was subsequently validated by using ternary configurations. Finally, the developed ML model was used to predict the formation energies of all possible configurations.

The objectives of this study are as follows: (i) to establish high-throughput first-principles calculations and ML method for computing and predicting the formation energy of the μ phase; (ii) to create a data set consisting of all binary and ternary configurations of formation energy data; and (iii) to provide a user-friendly graphical user interface (GUI) presenting the ML model constructed based on high-throughput first-principles calculations from this study, enabling easy access to the formation energy of the μ phase for interested individuals.

2. CALCULATION MODELS AND METHODS

2.1. Atomic Model. The μ phase belongs to TCP, and its space group is $R\bar{3}m$ (No. 166).[25] To elucidate the atomic interactions within the μ phase, it is commonly described using its equivalent structure, $A_{21}B_{18}$, characterized by a hexagonal
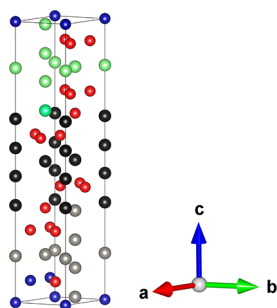
Figure 1. Hexagonal crystal structure of the μ phase with five distinct sites: 3a (blue), $6c_1$ (gray), $6c_2$ (black), $6c_3$ (green), and 18h (red).[24,25]

lattice structure containing 39 atoms distributed among five distinct lattice sites, as shown in Figure 1, where different colors represent different sites. The lattice parameters of the μ phase are $a = 4.72 \sim 4.80$ Å, $c = 25.679 \sim 25.90$ Å, $\alpha = 90°$, $\beta = 90°$, $\gamma = 120°$.[24] It consists of coordination polyhedra with coordination numbers of 12, 14, 15, and 16, thereby encompassing all types of coordination polyhedra characteristic of TCP structures.[31]

2.2. First-Principles Calculations. All calculations in this study were performed using the Vienna ab initio simulation package (VASP).[32,33] The electron−electron interactions were described using the projector-augmented wave (PAW)[34] method with a cutoff energy of 450 eV. The generalized gradient approximation (GGA) with the Perdew−Burke−Ernzerhof (PBE)[35] exchange−correlation functional was employed to account for exchange−correlation effects. The Monkhorst−Pack scheme[36] was utilized to generate a k-point mesh with a resolution of $7 \times 7 \times 1$. The convergence criteria for electronic self-consistency were set to 1×10^{-5} eV/atom. Following the structural optimization, the forces acting on each atom were required to be less than 0.02 eV/Å. Due to the presence of some magnetic elements, spin polarization is considered in this study.

The energy−volume ($E−V$) data obtained from first-principles calculations were fitted to the four-parameter Birch−Murnaghan equation of state (EOS). This fitting process aimed to estimate the equilibrium total energy (E_0) and the equilibrium volume (V_0).

$$E(V) = a + bV^{-2/3} + cV^{-4/3} + dV^{-6/3} \tag{1}$$

where a, b, c, and d are the fitting parameters. More comprehensive information can be found in refs 37 and 38.

Formation energy refers to the energy associated with the formation or generation of a substance. It is an important concept in the fields of materials science and chemistry used to describe and assess the stability and formation processes of compounds, crystals, molecules, and other substances. In this study, the ML model was constructed based on computed formation energies. The computation of formation energy is carried out with the following equation[39]:

$$E_f = \frac{E(\mu) - 3E_i - 6E_j - 6E_k - 6E_l - 18E_m}{39} \tag{2}$$

where $E(\mu)$ represents the total energy of the μ phase. The symbols E_i, E_j, E_k, E_l, and E_m denote the total energy per atom in their ground state at the 3a, $6c_1$, $6c_2$, $6c_3$, and 18h sites, respectively.

2.3. Elastic Properties. Typically, the elastic constants C_{ij} reflect the response of materials to external forces. In this study, the elastic constants were calculated based on the stress−strain method.[40] This method involves specifying lattice vectors R in Cartesian coordinates and applying a set of normal strains (ε_1, ε_2, and ε_3) and shear strains (ε_4, ε_5, and ε_6) to the crystal. The formula is as follows:

$$R = \begin{bmatrix} a_1 & a_2 & a_3 \\ b_1 & b_2 & b_3 \\ c_1 & c_2 & c_3 \end{bmatrix} \begin{bmatrix} 1 + \varepsilon_1 & \varepsilon_6/2 & \varepsilon_5/2 \\ \varepsilon_6/2 & 1 + \varepsilon_2 & \varepsilon_4/2 \\ \varepsilon_5/2 & \varepsilon_4/2 & 1 + \varepsilon_3 \end{bmatrix} \tag{3}$$

where $\bar{a} = (a_1, a_2, a_3)$, $\bar{b} = (b_1, b_2, b_3)$, and $\bar{c} = (c_1, c_2, c_3)$ represent the lattice vector.

Then, the linearly independent sets of strains are applied as follows:
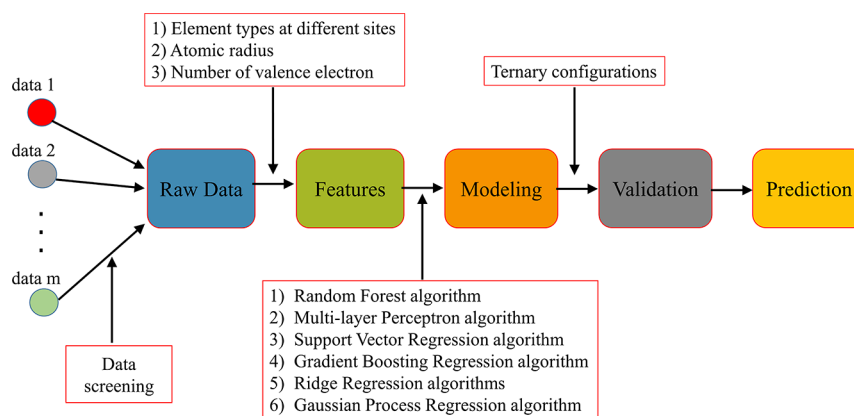
Figure 2. Machine learning workflow in this study.

$$\begin{bmatrix} s & 0 & 0 & 0 & 0 & 0 \\ 0 & s & 0 & 0 & 0 & 0 \\ 0 & 0 & s & 0 & 0 & 0 \\ 0 & 0 & 0 & s & 0 & 0 \\ 0 & 0 & 0 & 0 & s & 0 \\ 0 & 0 & 0 & 0 & 0 & s \end{bmatrix} \tag{4}$$

where s represents the applied strain values in different directions, with s set to ± 0.01. The results obtained from first-principles calculations yield the corresponding stresses $\sigma = \sigma_1$, σ_2, σ_3, σ_4, σ_5, and σ_6 for the deformed structure. According to the generalized Hooke's law, the elastic matrix C_{ij} can be determined as follows:

$$\begin{bmatrix} C_{11} & C_{12} & C_{13} & 0 & 0 & 0 \\ C_{12} & C_{11} & C_{13} & 0 & 0 & 0 \\ C_{13} & C_{13} & C_{33} & 0 & 0 & 0 \\ 0 & 0 & 0 & C_{44} & 0 & 0 \\ 0 & 0 & 0 & 0 & C_{44} & 0 \\ 0 & 0 & 0 & 0 & 0 & \dfrac{(C_{11}-C_{12})}{2} \end{bmatrix} = \varepsilon^{-1}\sigma \tag{5}$$

The μ phase in the hexagonal structure is characterized by five independent elastic constants (C_{11}, C_{12}, C_{13}, C_{33}, and C_{44}, $C_{66} = \frac{(C_{11}-C_{12})}{2}$). The bulk modulus ($B$), shear modulus ($G$), Young's modulus ($E$), and the ratio B/G can be calculated using the Voigt−Reuss−Hill (VRH) approach. For the hexagonal system, the Voigt and Reuss bounds of B_V, G_V, B_R, and G_R can be described as follows[41]:

$$B_V = \frac{1}{9}[2(C_{11} + C_{12}) + C_{33} + 4C_{13}] \tag{6}$$

$$B_R = \frac{(C_{11} + C_{12})C_{33} - 2C_{13}^2}{C_{11} + C_{12} + 2C_{33} - 4C_{13}} \tag{7}$$

$$G_V = \frac{1}{30}(7C_{11} - 5C_{12} + 12C_{44} + 2C_{33} - 4C_{13}) \tag{8}$$

$$G_R = \frac{5}{2}\left[\frac{((C_{11} + C_{12})C_{33} - 2C_{13}^2)C_{66}C_{44}}{3B_V C_{66}C_{44} + ((C_{11} + C_{12})C_{33} - 2C_{13}^2)(C_{44} + C_{66})}\right] \tag{9}$$

The expressions of bulk modulus (B), shear modulus (G), and Young's modulus (E) are

$$B = \frac{1}{2}(B_V + B_R) \tag{10}$$

$$G = \frac{1}{2}(G_V + G_R) \tag{11}$$

$$E = \frac{9BG}{3B + G} \tag{12}$$

2.4. Machine Learning Methods. Figure 2 illustrates the workflow of the ML method, which can be broadly divided into five steps: (i) data acquisition, (ii) feature extraction, (iii) ML model construction, (iv) validation, and (v) prediction for additional configurations. A brief overview of the key steps is provided below:

(1) Raw data: The data utilized in this study comprise the formation energy and lattice parameters of various configurations, obtained through first-principles high-throughput calculations. The investigation focuses on 12 elemental species, namely, Al, Co, Cr, Fe, Mn, Mo, Nb, Ni, Ta, W, Zn, and Zr. The selection of these elements was based on a thorough analysis of previous studies and the potential systems in which the μ phase could emerge.[31] The total number of configurations with these 12 elements is 248832 (12^5). However, considering the computational cost associated with first-principles calculations, the focus of this study was on a subset of binary and ternary configurations.

(2) Features: In this study, three features have been chosen—element types at different sites, atomic radius, and number of valence electrons. The selection of these features was carefully considered. It is well known that different elements exhibit distinct properties and stabilities in the μ phase. To address this, the first feature selected is the element types at different sites. The encoding technique of one-hot encoding is employed to represent the types of elements at each site, resulting in a 12-dimensional vector for each site. It is worth noting that the stability of the TCP phase is influenced by both geometric and electronic factors.[42] In addition, Pettifora et al.[21] have also investigated the influence of atomic size and electronic structure on the stability of the TCP phase, revealing significant impacts of both factors on its stability. We further selected the atomic radius and number of valence

Table 1. Comparison of the Calculated Lattice Parameters, Elastic Constants, and Elastic Modulus with Other Results

phase	methods	a (Å)	c (Å)	C_{11}	C_{12}	C_{13}	C_{33}	C_{44}	C_{66}	B (Gpa)	G (Gpa)	E (Gpa)
$Co_{21}W_{18}$	this work	4.748	25.584	507	198	159	564	119	154	289	147	378
	ref 24	4.768	25.647	514	200	157	566	119	157	291	148	380
	ref 25	4.747	25.580									

Table 2. Binary and Ternary Systems of Configurations Computed in This Study

binary systems	ternary systems
Al−Co, Al−Cr, Al−Fe, Al−Mo, Al−Nb, Al−Ta, Al−W, Al−Zn Co-Cr, Co−Fe, Co−Mn, Co−Mo, Co−Nb, Co−Ni, Co−Ta, Co−W, Co−Zn, Cr−Fe, Cr−Ta, Cr−W, Cr−Zn, Fe−Mo, Fe−W, Fe−Ta, Mn−Ta, Mo−Ta, Mo−W, Nb−Ni, Nb−Ta, Nb−W, Nb−Zn, Ni−Ta, Ni−W, Ta−W, Ta−Zn, W−Zn, W−Zr	Al−Co−Ta, Cr−Co−Ta, Co−Fe−Ta, Co−Mn−Ta, Co−Ni−Ta, Co−Ta−Zn

electrons as additional features. For each configuration, a $(12 + 2) \times 5 = 70$-dimensional vector was generated as its feature representation.

(3) Modeling: All ML models were implemented by using Python 3.9 with the scikit-learn 1.1 library. There are many machine learning algorithms, each with its own advantages and limitations, in terms of accuracy and speed. In this study, six different algorithms were employed to construct the ML models: random forest algorithm (RF),[43] multilayer perceptron algorithm (MLP),[44] support vector regression algorithm (SVR),[45] gradient boosting regression algorithm (GBR),[46] ridge regression algorithm (LR),[47] and Gaussian process regression algorithm (GPR).[48] To ensure the accurate and reliable evaluation of the ML model, two data-partitioning methods were employed: data set splitting into training and testing sets in an 8:2 ratio and the adoption of 10-fold cross-validation. These multifaceted evaluation strategies enable a comprehensive assessment of the model's performance and generalization capabilities. The hyperparameters for each ML model were determined by using grid search methods.

(4) Validation and prediction: After the ML models were constructed, the validation process involved using the computed ternary configuration data. Once the models' generalization ability was verified, they were used to predict data for all other configurations.

3. RESULTS

3.1. Elastic Constants and Elastic Moduli. The initial crystal structure employed in this study is $Co_{21}W_{18}$. To demonstrate the stability of the initial structure and validate the accuracy of the calculations, the lattice parameters, elastic constants, and elastic moduli were computed and compared with experimental values and those reported in previous studies.

The crystal structure of $Co_{21}W_{18}$ was optimized, and the optimized lattice parameters as well as the calculated bulk modulus (B), shear modulus (G), and Young's modulus (E) are reported in Table 1. Comparison of the computational results with the experimental data and findings from other studies reveals that the relative errors for both lattice parameters and elastic moduli are less than 1%, strongly suggesting the reasonableness of the computational results.

According to the Born stability criteria,[49] the hexagonal structure should satisfy the following conditions to demonstrate mechanical stability:[50] $C_{11} > 0$; $(C_{11} − C_{12}) > 0$; $(C_{11} + C_{12})C_{33} − 2C_{13}^2 > 0$; As seen in Table 1, these conditions are satisfied, indicating the mechanical stability of the hexagonal structure. Furthermore, the comparison of our computational results to

Table 3. Formation Energy (E_f, eV/atom) of All Configurations in the Co−Ta System and Computational Values from Other Studies

3a	6c$_1$	6c$_2$	6c$_3$	18h	E_f	ref 52
Co	Co	Co	Co	Co	0.12	0.12
Ta	Ta	Ta	Ta	Ta	0.12	0.11
Co	Ta	Co	Ta	Co	−0.07	−0.07
Co	Ta	Ta	Co	Co	−0.14	−0.14
Co	Ta	Ta	Ta	Co	−0.24	−0.24
Co	Co	Co	Ta	Ta	0.52	0.52
Co	Co	Ta	Co	Ta	0.22	0.23
Co	Co	Ta	Ta	Ta	0.32	0.33
Co	Ta	Co	Co	Ta	0.41	0.42
Co	Ta	Co	Ta	Ta	0.27	0.28
Co	Ta	Ta	Co	Ta	0.21	0.23
Ta	Co	Co	Ta	Co	0.05	0.06
Ta	Co	Ta	Co	Co	0.06	0.06
Ta	Co	Ta	Ta	Co	−0.03	−0.03
Ta	Ta	Co	Co	Co	0.05	0.05
Ta	Ta	Co	Ta	Co	−0.16	−0.16
Ta	Ta	Ta	Co	Co	−0.12	−0.12
Ta	Co	Co	Co	Ta	0.57	0.57
Ta	Co	Co	Ta	Ta	0.63	0.63
Ta	Co	Ta	Co	Ta	0.25	0.25
Co	Co	Co	Ta	Co	0.10	0.10
Co	Co	Ta	Co	Co	−0.01	−0.01
Co	Co	Ta	Ta	Co	−0.05	−0.05
Co	Ta	Co	Co	Co	0.08	0.07
Co	Co	Co	Co	Ta	0.44	0.44
Co	Ta	Ta	Ta	Ta	0.07	0.07
Ta	Co	Co	Co	Co	0.13	0.13
Ta	Ta	Ta	Ta	Co	−0.25	−0.26
Ta	Co	Ta	Ta	Ta	0.34	0.35
Ta	Ta	Co	Co	Ta	0.55	0.55
Ta	Ta	Co	Ta	Ta	0.43	0.44
Ta	Ta	Ta	Co	Ta	0.28	0.28

those reported by others shows minimal differences, confirming the accuracy of the calculations in this study.

B describes a material's resistance to volume change under an external pressure. A higher bulk modulus indicates a stronger resistance to deformation. G reflects a material's resistance to shape changes caused by shear strain. E is defined as the ratio of stress to strain and provides a measure of a solid material's stiffness. Based on the literature review, among the common binary μ phases ($Co_{21}W_{18}$, $Co_{21}Nb_{18}$, and $Co_{21}Mo_{18}$), $Co_{21}W_{18}$ exhibits the best mechanical performance. This further confirms the rationality of selecting the initial structure. The next step will
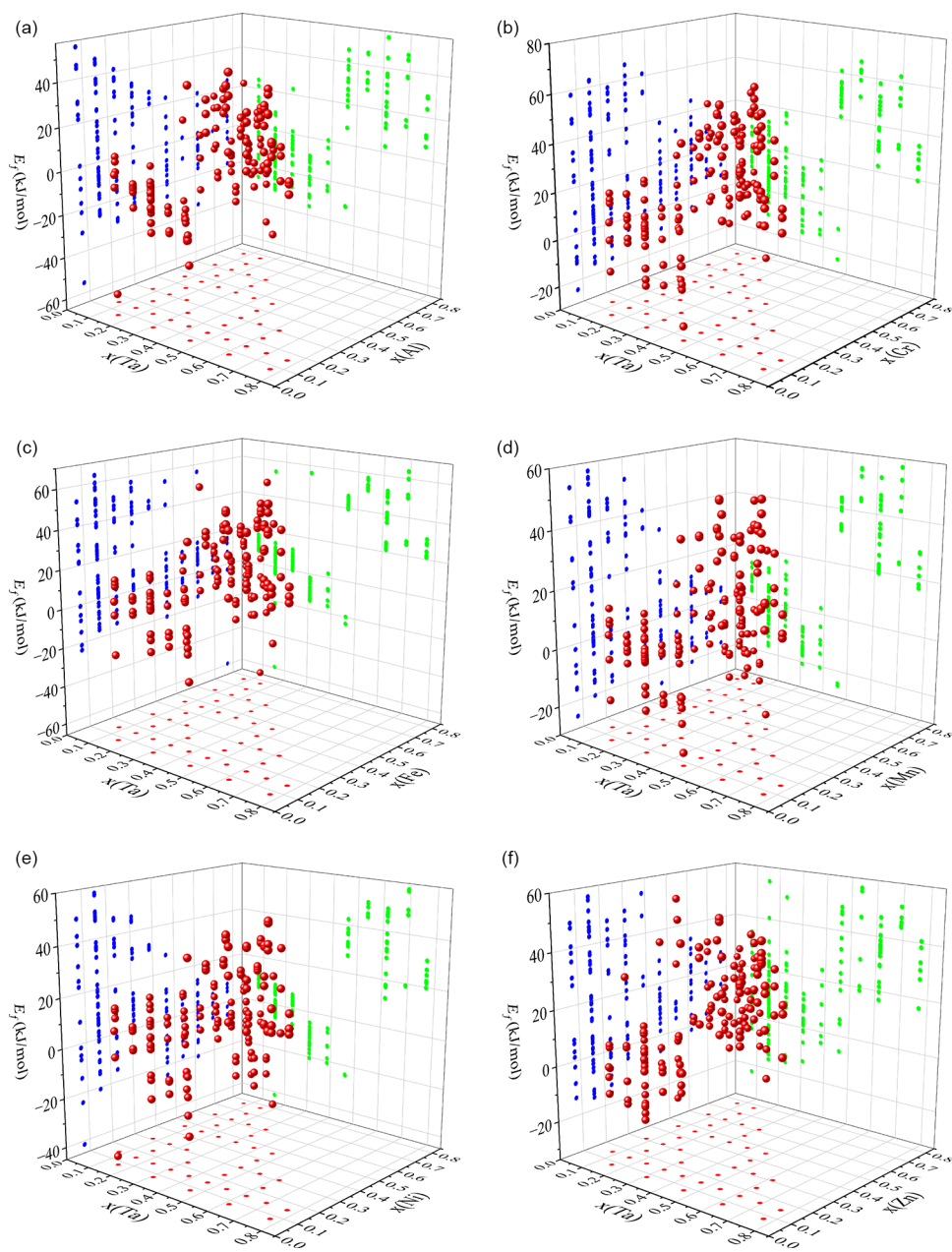
Figure 3. Ternary data used to validate machine learning models: (a) Al−Co−Ta, (b) Cr−Co−Ta, (c) Co−Fe−Ta, (d) Co−Mn−Ta, (e) Co−Ni−Ta, and (f) Co−Ta−Zn. The red balls represent the individual configurations, and the blue, green, and red circular planes represent the projections on the three surfaces.

involve utilizing this initial structure for first-principles high-throughput calculations.

3.2. Results of First-Principles Calculations. In this study, the formation energy data of 1036 binary configurations of the μ phase were computed to construct an ML model. Additionally, the formation energy data of 900 ternary configurations of the μ phase were calculated to validate the model's generalization ability. The computed binary configurations encompassed nearly all possible systems of the μ phase, while the ternary configurations included six systems: Al−Co−Ta, Cr−Co−Ta, Co−Fe−Ta, Co−Mn−Ta, Co−Ni−Ta, and Co−Ta−Zn (detailed in Table 2). Among these binary systems, the μ phase was reported existing in 11 different binary systems, namely Co−Mo, Fe−Mo, Co−Nb, Nb−Ni, Nb−Zn, Co−Ta,

Fe−Ta, Ni−Ta, Ta−Zn, Co−W, and Fe−W,[12,34] exhibiting thermodynamic stability.

For ML, the accuracy of the raw data is crucial as it directly influences the training and performance of the model. If the initial data contain errors or biases, the model will learn and incorporate those inaccuracies, leading to a decrease in its accuracy. Accurate initial data provide correct patterns and trends, which contribute to building an accurate model. To validate the accuracy of the computed formation energy data in this study, the configurations of the Co−Ta binary system were selected and compared with the literature data. The comparison results are presented in Table 3. It can be observed that the computed data highly align with the literature data, with 20 configurations exhibiting the same formation energy values. The maximum deviation observed was 0.02 eV/atom, indicating the
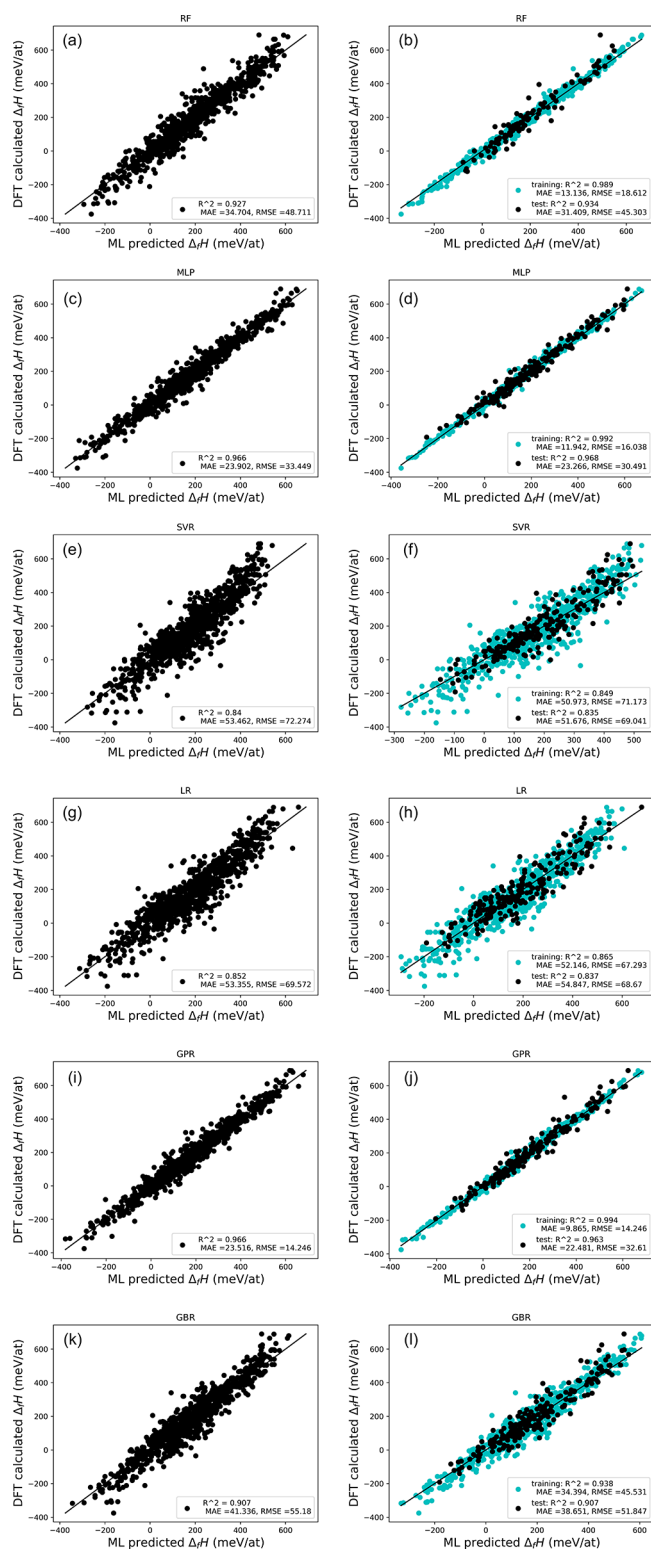
Figure 4. ML models constructed using six algorithms and different model evaluation methods: (a), (c), (e), (g), (i), and (k) were assessed using 10-fold cross-validation, while (b), (d), (f), (h), (j), and (l) followed an 8:2 ratio for training set to test set partitioning.

accuracy of the computed data. In addition, a portion of the data for the Co−Fe−Ta system has been utilized in experimental investigation and thermodynamic modeling of the Co−Fe−Ta system.[51] This specific data set has undergone cross-validation

through both the CALPHAD method and experimental techniques.

In ML, the training data are typically utilized to train the model, optimize its parameters, and learn the patterns and trends from the data. However, evaluating the model's performance solely based on training data is insufficient, as the model may overfit the training data, resulting in poor performance on new, unseen data. A validation data set, which is independently selected from the original data and mutually exclusive from the training and testing data sets, is essential for assessing the model's performance on unknown data. Once the model is trained, testing it on the validation data provides an objective evaluation of its performance.

By using the validation data, the model's generalization ability can be assessed, determining its accuracy in predicting unseen data. The validation data serve as an independent data set for evaluating and verifying the model's performance and generalization ability, playing a crucial role in model development and evaluation. The validation data set used in this study is illustrated in Figure 3.

3.3. Construction of the Machine Learning Model. In this study, we employed six algorithms to construct ML models, as described in Section 2.4. These six algorithms are RF, MLP, SVR, GBR, LR, and GPR. In order to evaluate the predictive performance of the ML models, several evaluation metrics were introduced. The commonly used metrics include the coefficient of determination (R^2), mean absolute error (MAE), root-mean-square error (RMSE), accuracy, recall, F1 score, and so on. These metrics are commonly used in regression problems to assess the performance of the models. However, the specific choice of the metric depends on the problem and requirements. R^2, MAE, and RMSE are all metrics used to measure the predictive ability of the models, and a smaller value (or closer to 1) for these metrics indicates a better model performance.

R^2 is a common metric used to measure the goodness of fit of a regression model to the data. It ranges from 0 to 1, where a value closer to 1 indicates the stronger ability of the model to explain the variability in the target variable. R^2 measures the overall fit of the model's predictions to the actual data, with 1 representing a perfect fit and 0 indicating that the model cannot explain the variance in the target variable. MAE is a metric used to measure the average absolute difference between the predictions of a regression model and actual values. It calculates the absolute difference between the predicted and actual values and then computes the average of these differences. A smaller MAE indicates a lower average difference between the model's predictions and the actual values, indicating a higher prediction accuracy. RMSE is a metric used to measure the square root of the average square difference between the predictions of a regression model and the actual values. It calculates the difference between the predicted and actual values, squares the differences, computes the average of these squared differences, and then takes the square root. RMSE considers both the magnitude and direction of the prediction errors, and a smaller value indicates higher prediction accuracy. The definitions of these metrics are as follows[53]:

$$R^2 = 1 - \frac{\sum_{i=1}^{n} (y_{\text{pre}} - y_i)^2}{\sum_{i=1}^{n} (y_i - \bar{y})^2} \tag{13}$$

$$\text{MAE} = \frac{1}{n} \sum_{i=1}^{n} |y_{\text{pre}} - y_i| \tag{14}$$

Table 4. Results Obtained from Different Model Evaluation Methods and Algorithms

algorithms	10-fold cross-validation	train: test = 8: 2
RF	R^2 = 0.927, MAE = 34.704 meV/atom, RMSE = 48.711 meV/atom	R^2 = 0.934, MAE = 31.409 meV/atom, RMSE = 45.303 meV/atom
MLP	R^2 = 0.966, MAE = 23.902 meV/atom, RMSE = 33.409 meV/atom	R^2 = 0.968, MAE = 23.266 meV/atom, RMSE = 30.491 meV/atom
SVR	R^2 = 0.84, MAE = 53.462 meV/atom, RMSE = 72.274 meV/atom	R^2 = 0.835, MAE = 51.676 meV/atom, RMSE = 69.041 meV/atom
LR	R^2 = 0.852, MAE = 53.355 meV/atom, RMSE = 69.572 meV/atom	R^2 = 0.837, MAE = 54.847 meV/atom, RMSE = 68.67 meV/atom
GPR	R^2 = 0.966, MAE = 23.516 meV/atom, RMSE = 14.246 meV/atom	R^2 = 0.963, MAE = 22.481 meV/atom, RMSE = 32.61 meV/atom
GBR	R^2 = 0.907, MAE = 41.336 meV/atom, RMSE = 55.18 meV/atom	R^2 = 0.907, MAE = 38.651 meV/atom, RMSE = 51.847 meV/atom

Table 5. Hyperparameter Selection for the Three Optimal Algorithms

ML algorithm	hyperparameters
RF	n_estimators = 80
	max_depth = 22
	min_samples_spilt = 2
MLP	hidden_layer_sizes = (100, 100, 100)
	activation = tanh
	max_iter = 1000
GPR	kernel = 1**2 * RBF
	n_restarts_optimizer = 20
	alpha = 5

$$RMSE = \sqrt{\frac{1}{n}\sum_{i=1}^{n}(y_{pre} - y_i)^2} \tag{15}$$

where y_{pre}, y_i, y_i, and n represent the predicted value, the true value, the mean of the true value, and the number of configurations, respectively.

Figure 4 illustrates the results of training and constructing models using the binary data in this study. Two model evaluation methods were employed, namely, 10-fold cross-validation and a training set to test set ratio of 8:2. Table 4 provides a clearer representation of the results. From the results above, it can be observed that among the two evaluation methods, the algorithms RF, MLP, and GPR achieved the highest accuracy. The hyperparameters used for these algorithms are listed in Table 5. The MAE values are 34.704/31.409, 23.902/23.266, and 23.516/22.481 meV/atom, respectively. In comparison to some previous studies,[54−57] which reported an MAE of approximately 50 meV/atom, the errors obtained in this research are significantly lower, indicating that the constructed models are effective in predicting the formation energy of the μ phase.

3.4. Validating the Generalization Ability of the Machine Learning Model. To verify the predictive capability of the model on unknown data, this study computed six sets of ternary data (as detailed in Table 2) for validation purposes. As mentioned above, the RF, MLP, and GPR algorithms demonstrated high accuracy. Therefore, the ML models constructed using these three algorithms were applied for validation. The validation results are presented in Figure 5. The results indicate that both the 10-fold cross-validation and the 8:2 training set to test set partitioning methods produced excellent results. Compared to the reported MAE of approximately 50 meV/atom from previous studies,[54−58] the models exhibited significantly lower errors even when applied to unseen ternary data. The MAE of the models was as follows: RF: 27.861/37.185 meV/atom; MLP: 32.754/22.61 meV/atom; and GPR: 30.319/17.166 meV/atom. These results demonstrate that the ML models constructed for the binary μ phase data in this study can

be effectively utilized for predicting the formation energy of ternary μ phases.

3.5. Prediction of Lattice Parameters. In DFT calculations, lattice parameters play a crucial role and are considered important in the structural optimization process. By adjusting the lattice parameters, one can explore the energy and stability of the different crystal structures. Optimizing the lattice parameters helps in finding the equilibrium structure of a system and determining the most stable crystal form. Providing an appropriate initial set of lattice parameters can significantly reduce the computational resources required for DFT calculations. Compared to using unreasonable lattice parameters, it can save about ∼10 times of the CPU consumption for the relaxation steps.[59]

The ML models constructed in this study can be applied not only to predict the formation energy but also to predict lattice parameters. To validate this viewpoint, we employed the RF and GBR algorithms in combination with 10-fold cross-validation to predict the lattice parameters. The results are shown in Figure 6. The data set used for lattice parameter validation included all available data, encompassing both binary and ternary data sets. The average value of the lattice parameter "a" in the data set was 5.013 Å, and the average value of lattice parameter "c" was 26.172 Å. The RF and GBR algorithms achieved MAE values of 0.024 and 0.029 Å, respectively, for lattice parameter "a", with error rates of only 0.479 and 0.578%. For lattice parameter "c", the MAE values were 0.214 and 0.234 Å, respectively, with error rates of only 0.817 and 0.894%. From these results, it is evident that besides formation energy, the ML models constructed in this study also perform well in predicting lattice parameters.

4. DISCUSSION

4.1. Comparison of Computational Time between DFT and ML Methods. Combining ML with DFT methods can significantly reduce the computation time and costs. To quantify the difference, we compared the required times for both approaches. Table 6 presents the comparison between the time needed for constructing ML models and making predictions using 10-fold cross-validation and the time required for performing DFT calculations alone. The ML approach requires training and testing sets to construct the models, which includes the time for DFT calculations on these sets. Once the ML model is constructed, it can be used to predict data from the validation set, resulting in a significant reduction in computation time and resources compared to using DFT calculations for the validation set data. The DFT calculations and ML were conducted on the High-Performance Computing Platform at Central South University. The computational tasks were executed on a robust configuration comprising two Intel Xeon Gold 6248R CPUs, each featuring 24 cores, thus providing a combined processing power of 48 cores. The system boasted a substantial 192 GB RAM capacity and utilized a 240 GB SSD for efficient data storage.
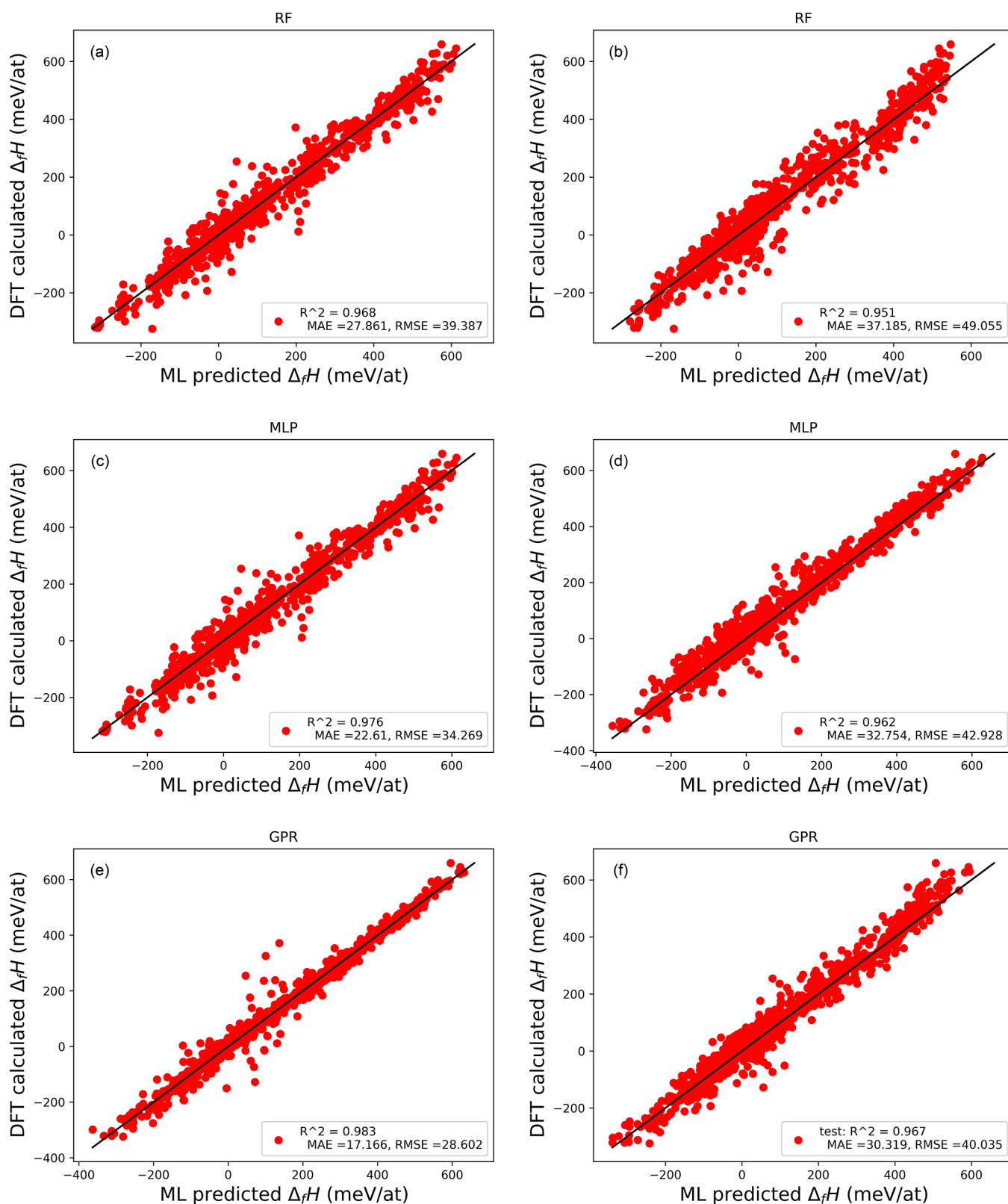
Figure 5. Predictive capabilities of the models on unknown data. (a−e) Results obtained from 10-fold cross-validation. (b−f) Results obtained from a training set to test set ratio of 8:2.

From Table 6, it can be observed that if DFT calculations were performed solely to obtain the validation sets, it would require 4320000 s. However, by combining ML methods to generate validation sets using the RF, MLP, and GPR algorithms, the respective time requirements are only 3.76, 12.9, and 226 s. With an accuracy that meets the criteria, this represents a reduction of at least 52% compared to DFT calculations alone, leading to a significant improvement in efficiency. The main reason for the long computation time in DFT calculations is the high computational complexity and the large computational work-
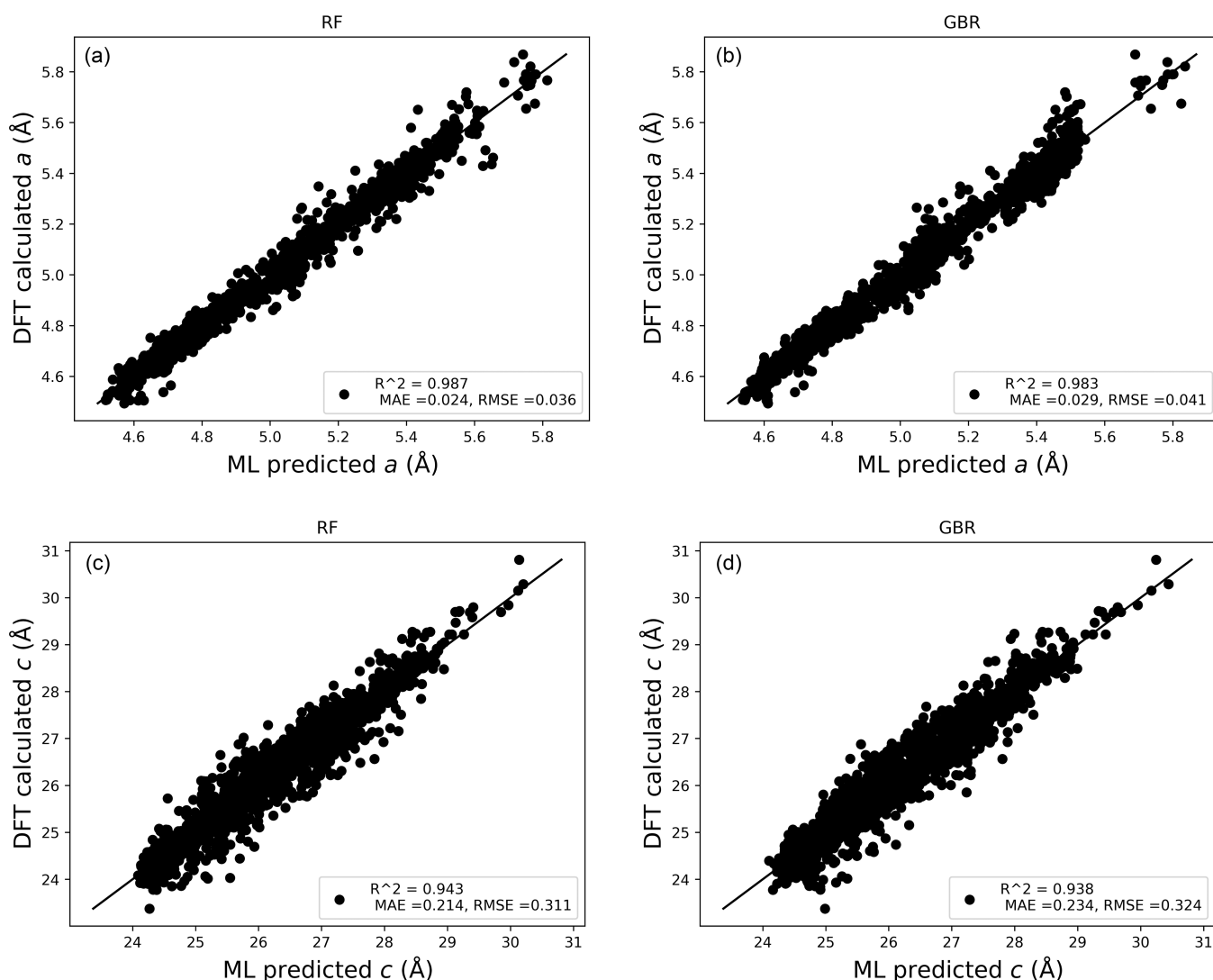
Figure 6. Prediction of lattice parameters *a* and *c* using different algorithms: (a, c) RF algorithm and (b, d) GBR algorithm.

Table 6. Comparison of Computational Time between Machine Learning and DFT Methods

methods	train and test sets (s)	validation sets (s)
DFT	3888121	4320000
RF	3888121	3.76
MLP	3888121	12.9
GPR	3888121	226

load. DFT methods involve detailed modeling and calculations of the electron behavior by solving the electronic wave functions and densities to describe the physical and chemical properties of materials. The electronic structure of each atom needs to be considered, and a significant amount of integration and iterative calculations is required, resulting in a significant increase in computation time. Through the synergy of ML and DFT calculations, it becomes possible to utilize ML models for fast predictions of material properties and behavior, thus greatly reducing the time and computational resources required for DFT calculations.

4.2. Feature Analysis of Models. The selection and design of appropriate features are of utmost importance in constructing accurate, efficient, and interpretable ML models. Appropriately chosen features can provide valuable information, differentiate

different samples, and play a crucial role in the model's training and prediction processes. Figure 7 presents the results of the model constructed using the RF algorithm with and without the inclusion of the atomic radius and number of valence electrons as additional features. From the results depicted in the figure, it can be observed that the model's predictive performance is superior when incorporating the additional features of atomic radius and number of valence electrons compared to the model without these features.

The atomic radius refers to the average distance between the atomic nucleus and its outermost electrons and exerts a significant influence on the formation energy of compounds. A smaller atomic radius generally implies that the outer electrons are closer to the atomic nucleus, leading to tighter and stronger chemical bonds between atoms. In the case of μ phase formation, this results in the release of more energy, thereby reducing the formation energy of the μ phase. On the contrary, a larger atomic radius leads to the formation of weaker chemical bonds, resulting in a relatively higher formation energy. The number of valence electrons, which represents the outermost electrons participating in chemical bonding, is also a key factor in the formation energy of compounds. A higher number of valence electrons typically indicates a greater number of electrons
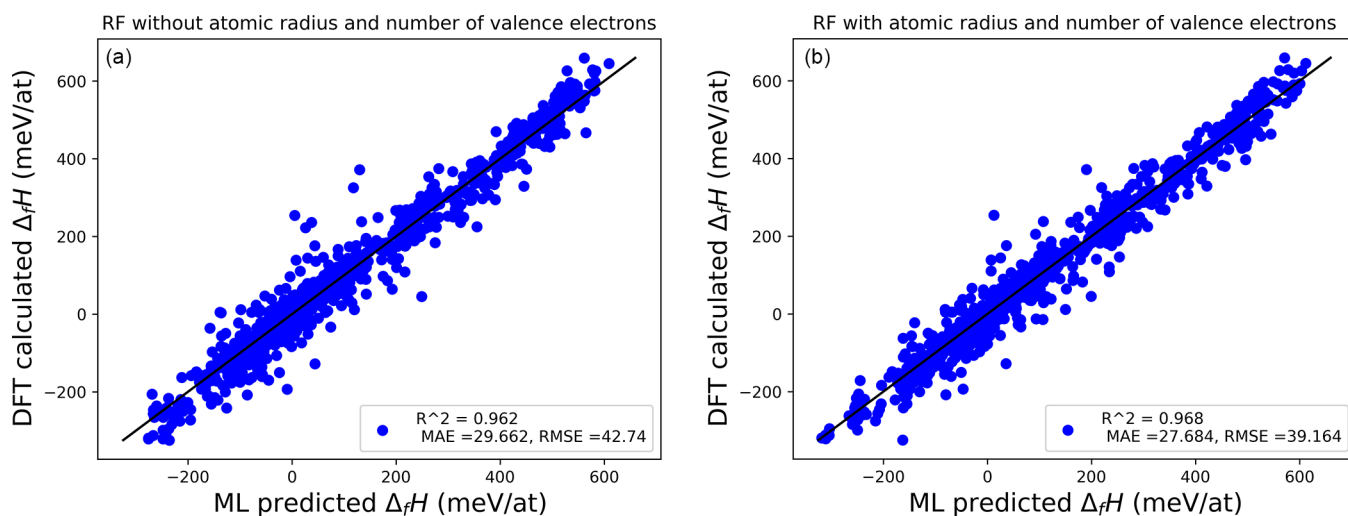
Figure 7. RF-predicted results: (a) without additional features and (b) with additional features.
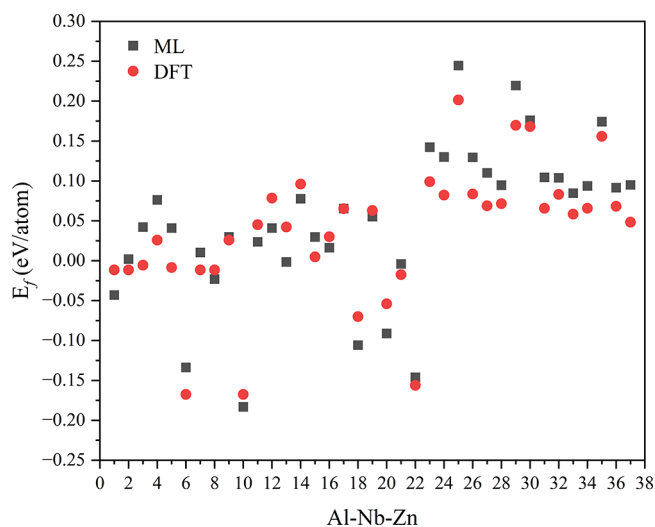

Figure 8. Comparison of DFT data and predicted results for a subset of the Al−Nb−Zn ternary system.

Figure 9. GUI developed for predicting the formation energy (kJ/mol) of the μ phase configurations.

available for chemical bond formation, thereby increasing the strength and stability of the chemical bonds. In the formation of the μ phase, a higher number of valence electrons facilitates the formation of stronger chemical bonds, thereby reducing the formation energy.

In summary, the selection of atomic radius and number of valence electrons as features for predicting the formation energy

of the μ phase is theoretically justified. The atomic radius reflects the strength and stability of chemical bonds, while the number of valence electrons provides information about the capability of chemical bond formation between atoms. Therefore, incorporating these two features as predictors of the μ phase formation energy helps capture the crucial factors influencing the formation energy and improves the accuracy and predictive capability of the model.

4.3. Prediction of Formation Enthalpy for All Ternary Configurations. To predict the formation energy data for all remaining ternary configurations, the ML model constructed using 10-fold cross-validation and the MLP algorithm was utilized. From the set of "Al, Co, Cr, Fe, Mn, Mo, Nb, Ni, Ta, W, Zn, and Zr", we randomly selected three elements, resulting in $C_{12}^3 = 220$ ternary systems. Excluding the six ternary systems used for validation, the formation energy data for 214 ternary systems was predicted. We randomly selected a subset of predicted data for the Al−Nb−Zn ternary system, supplemented by DFT calculations, and compared the results of the two methods. The results are presented in Figure 8.

Figure 8 displays different configurations represented by numerical values on the x-axis, with each number corresponding to a specific configuration. The y-axis represents the formation energy, whereas the black squares represent the ML-predicted values obtained in this study, and the red circles represent the values calculated using DFT. It is evident from the graph that the discrepancy between the two sets of values is minimal, with errors generally below 50 meV/atom. The previous analysis indicates that this level of error is acceptable and reasonable compared to previous reports. Particularly noteworthy is configuration number 17, where the ML-predicted value is 0.0653 eV/atom, while the DFT-computed value is 0.0652 eV/atom. The difference between the two is extremely small, and the graph illustrates that the two points almost coincide. In conclusion, the ML model accurately predicts the ternary data for all other configurations, and the constructed database can be considered reliable.

4.4. Practical Applications. To facilitate researchers in obtaining formation energy data for the μ phase and effectively using the constructed model, a Python-based GUI has been developed. Figure 9 displays the main interface. The GUI possesses characteristics of simplicity and user-friendliness, making it suitable for predicting the formation energy of all

configurations. Users only need to randomly select elements from the set including "Al, Co, Cr, Fe, Mn, Mo, Nb, Ni, Ta, W, Zn, and Zr" and fill in the corresponding five sites within the interface. By clicking 'Predict', users can obtain the corresponding formation energy data for the selected configuration. The GUI can be provided as request.

5. CONCLUSIONS

This study presents an innovative approach for predicting the formation energies of the μ phases. By utilizing our self-calculated DFT database, we constructed 12 ML models using six different algorithms and two model evaluation methods. The results demonstrate that the ML models not only exhibit high accuracy in predicting the formation energy of the μ phases but also perform well in predicting the lattice parameters.

The elements involved in this study include Al, Co, Cr, Fe, Mn, Mo, Nb, Ni, Ta, W, Zn, and Zr. The general strategy employed in this study was to construct models based on DFT-calculated binary data and validate them using DFT-calculated ternary data. Once satisfactory accuracy was achieved, the formation energies of all possible ternary configurations were predicted. Based on these analyses, the following conclusions can be drawn:

(1) The formation energies of 1036 binary configurations and 900 ternary configurations were calculated. A comparison with previous reports showed good agreement and high accuracy of the calculated results.

(2) Training the models using binary data yielded excellent performance. The RF, MLP, and GPR algorithms, combined with 10-fold cross-validation, achieved MAE values of 34.704, 23.902, and 23.516 meV/atom, respectively. Subsequently, the ML models of these three algorithms were validated using ternary data, resulting in MAE values of 27.861, 32.754, and 30.319 meV/atom, respectively. These results demonstrate that the ML models constructed in this study can effectively predict the formation energy of the μ phase.

(3) The application of the models to predict the lattice parameters of the μ phases yielded favorable results. The average values of "a" and "c" lattice parameters in the data set were 5.013 and 26.172 Å, respectively. The RF and GBR algorithms achieved MAE values of 0.024 and 0.029 Å for "a", with error rates of only 0.479 and 0.578%, respectively. For "c", the MAE values were 0.214 and 0.234 Å, with error rates of only 0.817 and 0.894%, respectively. These results indicate that, in addition to the formation energy, the ML models constructed in this study also perform well in predicting the lattice parameters.

(4) To predict the formation energy of all ternary data sets, excluding the validation data set, the constructed ML models were utilized. Furthermore, a user-friendly GUI was developed by using Python, enabling users to efficiently obtain the corresponding formation energy data.

■ AUTHOR INFORMATION

Corresponding Author

Jiong Wang − *State Key Laboratory of Powder Metallurgy, Central South University, Changsha 410083, China;* ⬤ orcid.org/0000-0003-1300-4804; Email: wangjionga@csu.edu.cn

Authors

Yue Su − *State Key Laboratory of Powder Metallurgy, Central South University, Changsha 410083, China*

You Zou − *Information and Network Center, Central South University, Changsha 410083, China*

Complete contact information is available at:
https://pubs.acs.org/10.1021/acsomega.3c05146

Notes

The authors declare no competing financial interest.

■ ACKNOWLEDGMENTS

■ REFERENCES

(1) Chen, B. Q.; Zhuo, L. C. Latest progress on refractory high entropy alloys: Composition, fabrication, post processing, performance, simulation and prospect. *Int. J. Refract. Met. Hard Mater.* **2023**, *110*, No. 105993.

(2) Maresca, F.; Curtin, W. A. Mechanistic origin of high strength in refractory BCC high entropy alloys up to 1900K. *Acta. Mater.* **2020**, *182*, 235−249.

(3) Pan, Y.; Chen, S. Influence of alloying elements on the mechanical and thermodynamic properties of ZrB_2 boride. *Vacuum* **2022**, *198*, No. 110898.

(4) Shahwaz, M.; Nath, P.; Sen, I. A critical review on the microstructure and mechanical properties correlation of additively manufactured nickel-based superalloys. *J. Alloys Compd.* **2022**, *907*, No. 164530.

(5) Guo, Z. M.; Zhang, A. J.; Han, J. S.; Meng, J. H. Effect of Si additions on microstructure and mechanical properties of refractory NbTaWMo high-entropy alloys. *J. Mater. Sci.* **2019**, *54* (7), 5844−5851.

(6) Chen, J.; Zhou, X. Y.; Wang, W. L.; Liu, B.; Lv, Y. K.; Yang, W.; Xu, D. P.; Liu, Y. A review on fundamental of high entropy alloys with promising high-temperature properties. *J. Alloys Compd.* **2018**, *760*, 15−30.

(7) Peng, Z.; Sun, J.; Luan, H. W.; Chen, N.; Yao, K. F. Effect of Mo on the high temperature oxidation behavior of $Al_{19}Fe_{20-x}Co_{20-x}Ni_{41}Mo_{2x}$ high entropy alloys. *Intermetallics* **2023**, *155*, No. 107845.

(8) Tarasov, D. A.; Milder, O. B.; Tiagunov, A. G. Modeling the influence of the composition of refractory elements on the heat resistance of nickel alloys by a deep learning artificial neural network. *Math. Methods Appl. Sci.* **2022**, *45* (15), 8809−8818.

(9) Wei, S. L.; Kim, S. J.; Kang, J.; Zhang, Y.; Zhang, Y. J.; Furuhara, T.; Park, E. S.; Tasan, C. C. Natural-mixing guided design of refractory high-entropy alloys with as-cast tensile ductility. *Nat. Mater.* **2020**, *19* (11), 1175−1181.

(10) Li, X. W.; Ding, R. G.; Wen, D. H.; Wang, Y.; Chu, M. Q.; Wang, L.; Zhang, P.; Zhang, S. Y. Microstructural evolution of a nickel-base single-crystal superalloy during high-temperature homogenisation. *Mater. Sci. Technol.* **2020**, *36* (18), 1936−1942.

(11) Xia, W. S.; Zhao, X. B.; Yue, L.; Zhang, Z. Microstructural evolution and creep mechanisms in Ni-based single crystal superalloys: A review. *J. Alloys Compd.* **2020**, *819*, No. 152954.

(12) Joubert, J. M.; Dupin, N. Mixed site occupancies in the μ phase. *Intermetallics* **2004**, *12* (12), 1373−1380.

(13) Cieslak, J.; Przewoznik, J.; Dubiel, S. M. Structural and electronic properties of the μ-phase Fe-Mo compounds. *J. Alloys Compd.* **2014**, *612*, 465−470.

(14) Schroeders, S.; Sandloebes, S.; Berkels, B.; Korte-Kerzel, S. On the structure of defects in the Fe_7Mo_6 μ-Phase. *Acta. Mater.* **2019**, *167*, 257−266.

(15) Yuan, Z. R.; He, Y. H.; Xie, F. W.; Kang, X. Y. Effects of Ti(C,N) additions on the microstructure and properties of the carbon-free high speed steel reinforced by intermetallic compounds. *Intermetallics* **2023**, *152*, No. 107767.

(16) Stewart, C. A.; Murray, S. P.; Suzuki, A.; Pollock, T. M.; Levi, C. G. Accelerated discovery of oxidation resistant CoNi-base γ/γ' alloys with high $L1_2$ solvus and low density. *Mater. Des.* **2020**, *189*, No. 108445.

(17) Olson, G.; Liu, Z.-K. Genomic Materials Design: CALculation of PHAse Dynamics. *Calphad* **2023**, *82*, No. 102590.

(18) Wang, P.; Peters, M. C.; Kattner, U. R.; Choudhary, K.; Olson, G. B. Thermodynamic analysis of the topologically close packed a phase in the Co-Cr system. *Intermetallics* **2019**, *105*, 13−20.

(19) Liu, Z.-K. Thermodynamics and its prediction and CALPHAD modeling: Review, state of the art, and perspectives. *Calphad* **2023**, *82*, No. 102580.

(20) Liu, Z.-K. Computational thermodynamics and its applications. *Acta. Mater.* **2020**, *200*, 745−792.

(21) Pettifor, D. G.; Seiser, B.; Margine, E. R.; Kolmogorov, A. N.; Drautz, R. Size versus electronic factors in transition metal carbide and TCP phase stability. *Philos. Mag.* **2013**, *93* (28−30), 3907−3924.

(22) Kaplan, B.; Blomqvist, A.; Selleby, M.; Norgren, S. Thermodynamic analysis of the W-Co-Cr system supported by ab initio calculations and verified with quaternary data. *Calphad* **2015**, *50*, 59−67.

(23) Wang, P. S.; Kontsevoi, O. Y.; Olson, G. B. Thermodynamic analysis of the Co-W system. *J. Mater. Sci.* **2019**, *54* (14), 10261−10269.

(24) Li, P.; Zhang, J. X.; Ma, S. Y.; Zhang, Y. J.; Jin, H. X.; Mao, S. C. First-principles investigations on structural stability, elastic and electronic properties of Co_7M_6 (M= W, Mo, Nb) μ phases. *Mol. Simul.* **2019**, *45* (9), 752−758.

(25) Zhao, M. X.; Huang, H. D.; Tang, T. T.; Li, X. B. First-principles study on the preferential sites of Cr in Co_7W_6. *Mater. Res. Express* **2023**, *10* (3), No. 036502.

(26) Hillert, M. The compound energy formalism. *J. Alloys Compd.* **2001**, *320* (2), 161−176.

(27) Kadulkar, S.; Sherman, Z. M.; Ganesan, V.; Truskett, T. M. Machine Learning-Assisted Design of Material Properties. *Annu. Rev. Chem. Biomol. Eng.* **2022**, *13*, 235−254.

(28) Liu, Y. L.; Niu, C.; Wang, Z.; Gan, Y.; Zhu, Y.; Sun, S. H.; Shen, T. Machine learning in materials genome initiative: A review. *J. Mater. Sci. Technol.* **2020**, *57*, 113−122.

(29) Schmidt, J.; Marques, M. R. G.; Botti, S.; Marques, M. A. L. Recent advances and applications of machine learning in solid-state materials science. *npj Comput. Mater.* **2019**, *5*, 83.

(30) Zhong, X.; Gallagher, B.; Liu, S.; Kailkhura, B.; Hiszpanski, A.; Han, T. Y.-J. Explainable machine learning in materials science. *npj Comput. Mater.* **2022**, *8* (1), 204.

(31) Wu, X. Z.; Liu, W.; Lu, X. G.; Jiang, Y. S.; He, Y. Site occupancy behavior of the binary μ phase. *J. Solid State Chem.* **2022**, *305*, No. 122704.

(32) Kresse; Furthmuller. Efficient iterative schemes for ab initio total-energy calculations using a plane-wave basis set. *Phys. Rev. B* **1996**, *54* (16), 11169−11186.

(33) Kresse, G.; Furthmuller, J. Efficiency of ab-initio total energy calculations for metals and semiconductors using a plane-wave basis set. *Comput. Mater. Sci.* **1996**, *1*, 6.

(34) Blochl. Projector augmented-wave method. *Phys. Rev. B* **1994**, *50* (24), 17953−17979.

(35) Perdew; Burke; Ernzerhof. Generalized Gradient Approximation Made Simple. *Phys. Rev. Lett.* **1996**, *77* (18), 3865−3868.

(36) Froyen. Brillouin-zone integration by Fourier quadrature: Special points for superlattice and supercell calculations. *Phys. Rev. B* **1989**, *39* (5), 3168−3172.

(37) Shang, S. L.; Saengdeejing, A.; Mei, Z. G.; Kim, D. E.; Zhang, H.; Ganeshan, S.; Wang, Y.; Liu, Z. K. First-principles calculations of pure elements: Equations of state and elastic stiffness constants. *Comput. Mater. Sci.* **2010**, *48* (4), 813−826.

(38) Wang, J.; Shang, S. L.; Wang, Y.; Mei, Z. G.; Liang, Y. F.; Du, Y.; Liu, Z. K. First-principles calculations of binary Al compounds: Enthalpies of formation and elastic properties. *Calphad* **2011**, *35* (4), 562−573.

(39) Su, Y.; He, S. Z.; Wang, J.; Zhang, D. L.; Wu, Q. First-Principles Study on Structure and Stability of GP Zones in Al-Mg-Si(-Cu) Alloy. *Materials* **2023**, *16* (11), 3897.

(40) Shang, S. L.; Wang, Y.; Liu, Z. K. First-principles elastic constants of α - and θ - Al_2O_3. *Appl. Phys. Lett.* **2007**, *90* (10), 101909.

(41) Hill, R. The elastic behavior of crystalline aggregate. *Proc. Phys. Soc. A* **1952**, *65* (5), 349.

(42) Joubert, J. M. Crystal chemistry and Calphad modeling of the σ phase. *Prog. Mater. Sci.* **2008**, *53* (3), 528−583.

(43) Breiman, L. Random forests. *Mach. Learn.* **2001**, *45* (1), 5−32.

(44) Popescu, M.-C.; Balas, V. E.; Perescu-Popescu, L.; Mastorakis, N. Multilayer perceptron and neural networks. *WSEAS Trans. Circuits Syst.* **2009**, *8* (7), 579−588.

(45) Smola, A. J.; Schölkopf, B. A tutorial on support vector regression. *Stat. Comput.* **2004**, *14*, 199−222.

(46) Bentéjac, C.; Csörgő, A.; Martínez-Muñoz, G. A comparative analysis of gradient boosting algorithms. *Artif. Intell. Rev.* **2021**, *54*, 1937−1967.

(47) McDonald, G. C. Ridge regression. *Wiley Interdiscip. Rev.: Comput. Stat.* **2009**, *1* (1), 93−100.

(48) Schulz, E.; Speekenbrink, M.; Krause, A. A tutorial on Gaussian process regression: Modelling, exploring, and exploiting functions. *J. Math. Psychol.* **2018**, *85*, 1−16.

(49) Born, M.; Huang, K. *Dynamical Theory of Crystal Lattices*; Oxford University Press: Oxford, 1988.

(50) Mouhat, F.; Coudert, F. X. Necessary and sufficient elastic stability conditions in various crystal systems. *Phys. Rev. B* **2014**, *90* (22), No. 224104.

(51) Wang, J.; Zhou, J.; Yang, W.; Huang, X.; Liu, K.; Wang, P.; Xu, H. The stability and homogeneity range of the TCP phases in the Co-Fe-Ta system. *Mater. Charact.* in revision.

(52) Wang, P. S.; Kossmann, J.; Kattner, U. R.; Palumbo, M.; Hammerschmidt, T.; Olson, G. B. Thermodynamic assessment of the Co-Ta system. *Calphad* **2019**, *64*, 205−212.

(53) Guo, J.; Xiao, B.; Li, Y. H.; Zhai, D.; Tang, Y. C.; Du, W.; Liu, Y. Machine learning aided first-principles studies of structure stability of Co_3(Al, X) doped with transition metal elements. *Comput. Mater. Sci.* **2021**, *200*, No. 110787.

(54) Kirklin, S.; Saal, J. E.; Meredig, B.; Thompson, A.; Doak, J. W.; Aykol, M.; Ruhl, S.; Wolverton, C. The Open Quantum Materials Database (OQMD): assessing the accuracy of DFT formation energies. *npj Comput. Mater.* **2015**, *1*, 15010.

(55) Jha, D.; Ward, L.; Paul, A.; Liao, W. K.; Choudhary, A.; Wolverton, C.; Agrawal, A. ElemNet: Deep Learning the Chemistry of Materials From Only Elemental Composition. *Sci. Rep.* **2018**, *8*, 17593.

(56) Ubaru, S.; Miedlar, A.; Saad, Y.; Chelikowsky, J. R. Formation enthalpies for transition metal alloys using machine learning. *Phys. Rev. B* **2017**, *95* (21), No. 214102.

(57) Zhang, Z. H.; Li, M.; Flores, K.; Mishra, R. Machine learning formation enthalpies of intermetallics. *J. Appl. Phys.* **2020**, *128* (10), 105103.

(58) Su, Y.; Wang, J. Machine learning aided High-throughput first-principles calculations to predict the formation enthalpy of σ phase. *Calphad* **2023**, *82*, No. 102599.

(59) Crivello, J. C.; Joubert, J. M.; Sokolovska, N. Supervised deep learning prediction of the formation enthalpy of complex phases using a DFT database: The σ-phase as an example. *Comput. Mater. Sci.* **2022**, *201*, No. 110864.